



**HAL**  
open science

# Tectono-thermal history of the intraplate San Bernardo fold and thrust belt in central Patagonia inferred by low-temperature thermochronology

Marie Genge, Alexis Derycke, Cécile Gautheron, Massimiliano Zattin, César Witt, Stefano Mazzoli, Xavier Quidelleur

## ► To cite this version:

Marie Genge, Alexis Derycke, Cécile Gautheron, Massimiliano Zattin, César Witt, et al.. Tectono-thermal history of the intraplate San Bernardo fold and thrust belt in central Patagonia inferred by low-temperature thermochronology. *Journal of South American Earth Sciences*, 2021, 109, 10.1016/j.jsames.2021.103333 . insu-03664864

**HAL Id: insu-03664864**

**<https://insu.hal.science/insu-03664864>**

Submitted on 24 Apr 2023

**HAL** is a multi-disciplinary open access archive for the deposit and dissemination of scientific research documents, whether they are published or not. The documents may come from teaching and research institutions in France or abroad, or from public or private research centers.

L'archive ouverte pluridisciplinaire **HAL**, est destinée au dépôt et à la diffusion de documents scientifiques de niveau recherche, publiés ou non, émanant des établissements d'enseignement et de recherche français ou étrangers, des laboratoires publics ou privés.



Distributed under a Creative Commons Attribution - NonCommercial | 4.0 International License

## **Tectono-thermal history of the intraplate San Bernardo Fold and Thrust Belt in central Patagonia inferred by low-temperature thermochronology**

Marie Genge<sup>1,2\*</sup>, Alexis Derycke<sup>3</sup>, Cécile Gautheron<sup>3</sup>, Massimiliano Zattin<sup>1</sup>, César Witt<sup>2</sup>, Stefano Mazzoli<sup>4</sup>, Xavier Quidelleur<sup>3</sup>

<sup>1</sup> Dipartimento di Geoscienze, Università degli Studi di Padova, via G. Gradenigo 6, 35131 Padova, Italy

<sup>2</sup> Univ. Lille, CNRS, Univ. Littoral Côte d'Opale, UMR 8187, LOG, Laboratoire d'Océanologie et de Géosciences, F 59000 Lille, France

<sup>3</sup> Université Paris-Saclay, CNRS, GEOPS, 91405, Orsay, France

<sup>4</sup> School of Science and Technology, Geology Division, University of Camerino, Italy

\*corresponding author

## **1. Abstract**

First low-temperature thermochronology data across the central Patagonia and thermal modeling provide information on the thermal history of the intraplate San Bernardo fold and thrust belt (44 - 46 °S). Apatite (U-Th-Sm)/He (AHe), fission tracks (AFT) ages and inverse thermal modeling indicate that the sedimentary rocks presently at the surface of the southwestern San Bernardo FTB have experienced a broadly similar thermal history: i) cooling at the deposition time during the Cretaceous, ii) a significant Eocene – early Miocene thermal event which totally reset the AHe data and partially the AFT data, and iii) a cooling since the early Miocene. Although former thermochronology studies in surrounding areas do not evidence any Neogene thermal event, our regionally consistent ages and thermal modeling most likely indicate a large-scale thermal event through the Eocene to the early Miocene. As sedimentary burial was not significant in this area through the Cenozoic, we propose that this heating episode might have been caused by coeval widespread and long-term intraplate volcanic processes associated with a modest burial and the increase of the geothermal gradient in the entire area, which has been strong enough to significantly affect the low-temperature thermochronometers regionally. A subsequent slow cooling phase starting from early Miocene may have been related with the termination of this intraplate volcanic phase and subsequent decrease of the thermal gradient to average values, and with a modest exhumation of ~1 km at most related to a mild deformation episode of the broken foreland and dynamic topography processes during the middle-late Miocene, as well as the weathering of the Oligo-Miocene basalts.

## **2. Introduction**

Intraplate contractional belts are enigmatic features, developed far from the orogen due to the reactivation of upper plate weaknesses mostly perpendicular to the main compressional stress during orogenic shortening. Some examples include the Iberian Chain (Guimerá and Alvaro, 1990; Guimerà Rosso, 2018), the Yinshan fold-and-thrust belt (Davis *et al.*, 1998; Lin *et al.*, 2013), the Laramide (Blackstone, 1980; Yonkee and Weil, 2015) and the Arabia-Eurasia collision zone (Cavazza *et al.*, 2019). The external part of the north-central Patagonian Andes is also related with a conspicuous NNW-trending intraplate belt named the San Bernardo fold and thrust belt (FTB), and interpreted as the central segment of the Patagonian Broken Foreland (Homoc *et al.*, 1995; Peroni *et al.*, 1995; Gianni *et al.*, 2015). This work aims to understand the thermal evolution of this contractional feature extended between 44 and 46 °S (Figure 1A). This intraplate belt, characterized by wide asymmetrical anticlines associated with WNW – ESE striking normal faults and NNE – SSW inverted normal faults, was built by several contraction episodes. The earliest compressive stage is recorded during the late Early Cretaceous and may have been sustained until the middle Eocene as evidenced by the synorogenic character of the Cretaceous – middle Eocene sedimentary formations exposed across the San Bernardo FTB (Barcat *et al.*, 1989; Suarez *et al.*, 2009; Navarrete *et al.*, 2015; Gianni *et al.*, 2017). Neogene and Quaternary deformation episodes are also recognized for the intraplate belt (Gianni *et al.*, 2015). The topographic growth of the San Bernardo FTB is directly related to the uplift of former depocenters enhanced by the reactivation of NNW-trending faults (Homoc *et al.*, 1995; Peroni *et al.*, 1995; Navarrete *et al.*, 2015). These structural inheritances acted as anisotropies focalizing strain during compression ~500 km away from the trench (Navarrete *et al.*, 2015). To unravel the significance of these deformational stages, still debated, we analyzed low-temperature thermochronology from the syntectonic Cretaceous deposits exposed across the southwestern San Bernardo FTB. Low-temperature thermochronological ages can record the signal of diverse thermal events which

may be related to significant sedimentary burial (Brandon *et al.*, 1998), magmatism (Calk and Naeser, 1973; Roy *et al.*, 2004), faulting (Ehlers *et al.*, 2001), or exhumation related to erosion processes (Willett *et al.*, 2003; Malusà *et al.*, 2005). The southwestern San Bernardo FTB represents a valuable natural laboratory to study the effect of burial, denudation and volcanism. Indeed, three main intraplate magmatism events occurred during the Eocene, from the late Oligocene to the early Miocene and during the Pliocene, which are related to periods of tectonic quiescence across the study area (Bruni *et al.*, 2008; Gianni *et al.*, 2015). In this work, we will mostly focus on apatite fission tracks (AFT) and (U-Th-Sm)/He (AHe) data. The latter allows identifying an early Miocene cooling event, whose interpretation could be either related to tectonic and associated denudation, or volcanism processes in this area.

### **3. Geological setting**

The San Bernardo FTB represents an intraplate belt into the central Patagonian foreland at ~44 - 46°S. This NNW-SSE trending broken foreland was initiated through several contraction episodes that reactivated inherited faults and generated deformation of former depocenters (Homovic *et al.*, 1995). The magmatic-metamorphic basement is buried below thick Jurassic to Lower Cretaceous volcano-sedimentary sequences deposited in half-graben systems (Figari *et al.*, 2016; Allard *et al.*, 2020 and references therein). These deposits are topped by a regional unconformity overlain by the late Lower – Upper Cretaceous Chubut Group, mainly exposed across the southern San Bernardo FTB. Initial sedimentation of the continental Chubut Group is represented by the Aptian Matasiete Formation, interfingering to the east with the Pozo D-129 Formation (e.g. Sciutto, 1981; Paredes *et al.*, 2007; Carignano *et al.*, 2017). Both units are overlain by the Aptian – Albian Castillo Formation (e.g. Lesta and Ferello, 1972; Suarez *et al.*, 2009; Tunik *et al.*, 2015), which is topped (locally

unconformably) by the fluvial members of the Bajo Barreal Formation assigned to Cenomanian – Coniacian (e.g. Hechem *et al.*, 1990; Umazano *et al.*, 2009). Thereby, the Laguna Palacios Formation and the Lago Colhué Huapi Formation (restricted to the western domain) represent the last fluvial infill of the Chubut Group to the Maastrichtian (e.g. Genise *et al.*, 2007; Casal *et al.*, 2015; Vallati *et al.*, 2016). They are unconformably covered by Paleogene successions stratigraphically arranged as follows: Danian – lower Paleocene marine Salamanca Formation restricted to the east due to the existence of positive reliefs at deposition time (e.g. Lesta *et al.*, 1980; Legarreta and Uliana, 1994); upper Paleocene – middle Eocene continental Rio Chico Formation (e.g. Foix *et al.*, 2013); and middle Eocene – lower Miocene tuffaceous Sarmiento Formation (e.g. Bellosi, 2010; Ré *et al.*, 2010). Neogene marine deposits recognized in the foreland basin (e.g. Chenque Formation) were not deposited across the southwestern San Bernardo FTB as this area already represented a topographic barrier during the Oligocene (Sciutto *et al.*, 2008; Barreda and Bellosi, 2014).

In the study area, the description of sediments belonging to the upper Chubut Group, the Salamanca and the Rio Chico Formations, evidence a late Early – Late Cretaceous and a Paleocene – middle Eocene deformation episodes acting in the intraplate belt (Navarrete *et al.*, 2015; Gianni *et al.*, 2015; Gianni *et al.*, 2017), while these formations appear mostly related to a syn-rift stage into the adjacent San Jorge Basin (Paredes *et al.*, 2013; Gianni *et al.*, 2015; Paredes *et al.*, 2018) and into the lower Chubut Group units (Allard *et al.*, 2020 and references therein). These Cretaceous – Paleogene contractional events are followed by a period of tectonic quiescence characterized by intraplate volcanism and modest foreland subsidence resulting from crustal thinning (Bruni *et al.*, 2008; Encinas *et al.*, 2018) which is related to slab rollback (Rapela and Kay, 1988; Echaurren *et al.*, 2016) after a reduction in average trench velocity (Maloney *et al.*, 2013). South and west of the Lago Musters (Figure 1A), Eocene alkaline sequences belonging to the San Bernardo Complex outcrop locally as

small intrusive gabbroic bodies associated with alkaline doleritic dikes (Pezzuchi and Fernández, 2001; Pezzuchi, 2018). Intraplate upper Oligocene – lower Miocene basalts, called the Buen Pasto Formation, whose origin is still debated (e.g. mantle plume, Kay *et al.*, 2007; asthenospheric upwelling, Bruni *et al.*, 2008; delamination, Remesal *et al.*, 2012), cap vast portions of the southern San Bernardo FTB, sometimes forming plateaus (Figure 1A). These basalts are also associated with moderate extensional processes as evidenced by coeval activity of minor normal faults (Bruni *et al.*, 2008; Gianni *et al.*, 2017). The Plio–Pleistocene Cerro Grande basalts lie unconformably above all the underlying formations and remain mostly undeformed (Figure 1E; Bruni *et al.*, 2008), unlike the Buen Pasto basaltic cover. Indeed, the Buen Pasto basaltic plateau has been affected by narrow NNW-trending folds with a maximum tilting of  $\sim 35^\circ$  (Figures 1A and 1D). This indicates that deformation processes were active across the broken foreland through the Miocene, between the deposition of the Buen Pasto and Cerro Grande basalts (Barcat *et al.*, 1989; Homocv *et al.*, 1995; Peroni *et al.*, 1995).

## Material and methods

Four Cretaceous tuffaceous sandstones were collected for apatite fission tracks and (U-Th-Sm)/He analysis in the southwestern San Bernardo FTB (MG7, MG9, MG17 and MG20; Figure 1A) in diverse formations of the Chubut Group (i.e. the Aptian Matasieta Formation, the Aptian – Albian Castillo Formation and the Cenomanian – Coniacian Bajo Barreal Formation; Figure 1B). Geographic location and stratigraphic age of the detrital samples are detailed in Table 1. In addition, two basalts were collected in this area for K-Ar dating: a tilted basalt MG18 (69.4250 °W, 45.0682 °S, 739 m) sampled in the Buen Pasto basalts and a basaltic dike MG21 (69.7130 °W, 45.4616 °S, 582 m) associated to the Cerro Grande basalts.

### 3.1. Apatite fission tracks

The apatite fission tracks (AFT) dating depends of the accumulation of linear damage in the apatite lattice due to the spontaneous fission decay of  $^{238}\text{U}$  into the crystal. The partial annealing zone (PAZ) corresponds to the interval ( $\sim 120 - 60^\circ\text{C}$ ) above which tracks are retained in the lattice (Green *et al.*, 1989). AFT have been counted in this study with the external detector method on the four Cretaceous detrital samples (Figures 1A and 1B). Apatite grains were separated from crushed rock samples at the University of Padua (Italy) using standard magnetic and heavy-liquid separation technique (Na-polytungstate with a density of  $2.8 \text{ g/cm}^3$ ). Apatite grains were then mounted in epoxy resin, polished and etched at 5.5M  $\text{HNO}_3$  during 20 seconds at  $20^\circ\text{C}$  to reveal spontaneous tracks. The mounts were covered by low-uranium muscovite foils, as external detector (Gleadow, 1981), and irradiated at the Radiation Center of Oregon State University with a nominal fluence of  $9 \times 10^{15}$  neutrons/cm<sup>2</sup>. After irradiation, mica detectors were etched for 40 minutes in 40% HF at  $20^\circ\text{C}$  to reveal induced tracks. We counted tracks and measured track length distribution using an Olympus optical microscope at a magnification of  $\times 1250$ . Age calculation and statistics were carried out with the Trackkey software (Dunkl, 2002). We report AFT ages as central age with  $1\sigma$  errors (Galbraith and Laslett, 1993), using a zeta calibration approach (Hurford and Green, 1983) with a zeta value of  $346 \pm 12$  for the CN5 dosimeter glass. Due to the small number of apatite extracted, the low U content and the few spontaneous tracks observed in most of the grains, no track lengths have been measured in these samples.

### 3.2. Apatite (U-Th-Sm)/He



The (U-Th-Sm)/He thermochronology method is based on the production, ejection and accumulation in the crystal of  $^4\text{He}$  gas produced by the alpha decay of radioactive elements ( $^{238}\text{U}$ ,  $^{235}\text{U}$ ,  $^{232}\text{Th}$ ,  $^{147}\text{Sm}$ ). As He is a gas, the accumulation in the crystal is thermo-dependent and will be a function of the time-temperature path, crystal size and diffusion coefficient that is strongly modified by the amount of radiation damage (Farley, 2000; Gautheron et al., 2009; Flowers et al., 2009). The partial retention zone (PRZ) is the interval above which He diffusivity is sufficiently low to retain He within the crystal. For apatite, the PRZ ranges approximately from 40 to 120°C depending on the thermal history and damage amount (Ault *et al.*, 2019 and references therein). We performed (U-Th-Sm)/He analysis at the University of Paris-Saclay (Orsay, France) on ten single grains from samples MG7, MG17 and MG20. After a careful selection (morphology, size, lack of visible inclusions, grain boundary phase), 2 to 4 apatite grains per sample (Figure 2) were placed individually into platinum baskets and heated twice by a diode laser ( $1030 \pm 50^\circ\text{C}$  for 5 min) for He-extraction. The  $^4\text{He}$  gas is mixed with a known  $^3\text{He}$  spike, purified and analyzed with a Prisma quadrupole mass spectrometer. These grains were then dissolved in a nitric acid solution (3 hours at  $70^\circ\text{C}$  in 50  $\mu\text{L}$   $\text{HNO}_3$  5N containing a known content of  $^{42}\text{Ca}$ ,  $^{235}\text{U}$ ,  $^{230}\text{Th}$ , and  $^{149}\text{Sm}$  followed by the addition of 0.9 mL ultrapure MQ water), before being analyzed with high resolution ICP mass spectrometry (Element XR from Thermo Scientific). Durango apatite fragments analyzed similarly were used for calibration. Single ages were corrected using the calculated ejection factor  $F_T$ , determined using the Monte Carlo simulation technique of Ketcham *et al.* (2011); the equivalent-sphere radius ( $R_s$ ) was calculated using the procedure of Gautheron and Tassan-Got (2010). The  $1\sigma$  error on single-grain AHe ages should be considered as 9%, reflecting the sum of errors in the ejection-factor correction and age dispersion of the standards. AHe analysis has been carried out on the Cretaceous samples, with the exception of the sample MG9, a poor-quality sample, for which no acceptable apatite crystals have been found.

### 3.3. K-Ar dating

In order to constrain the timing of the late deformation period in this area (e.g. Bruni *et al.*, 2008), a tilted basalt (MG18) and an undeformed basaltic dike related to the basaltic plateau (MG21) were collected in the San Bernardo FTB for K-Ar dating into the Oligo-Miocene Buen Pasto formation, and in the Pliocene Cerro Grande basalts, respectively. The K-Ar dating technique, which relies on the measurement of radiogenic argon ( $^{40}\text{Ar}^*$ ) content produced from the radioactive decay of  $^{40}\text{K}$ , has been applied here to the groundmass. As it is the last mineral phase to crystallize, this technique provides ages of the lava emplacement. Consequently, any inherited  $^{40}\text{Ar}$  carried by early crystallizing minerals, such as olivine, pyroxene, or plagioclase, are neglected (e.g. Samper *et al.*, 2008). Furthermore, this phase is enriched in incompatible elements including potassium, and it is believed to be in isotopic equilibrium with the atmosphere during cooling to surface temperature for subaerial lavas (e.g., Sharp *et al.*, 2005). From both samples, groundmass was separated within a 125-250  $\mu\text{m}$  size fraction, determined from thin section analyses (Figure 3). Following manual crushing and sieving, heavy liquids (diiodomethane) were used to extract groundmass within a narrow density range in order to remove any undetected weathered fraction. Both potassium and argon measurements were carried out in the GEOPS laboratory (Paris-Saclay University, France) by using the unspiked K-Ar Cassinot-Gillot technique (e.g. Gillot *et al.*, 2006). Decay constants and isotopic ratios of Steiger and Jäger (1977) have been used. The full description of analytical procedures, standards, age calculation and uncertainty calculation are given in Bablon *et al.* (2018).

## 4. Results

### 4.1. Partially reset AFT ages

Despite the low number of counted grains (10 to 53), Cretaceous samples yielded four consistent late Early – Late Cretaceous AFT ages between  $128.0 \pm 8.7$  Ma and  $88.5 \pm 11.4$  Ma. The chi-square probability ( $> 5\%$ ) indicates a single population for all the samples. The radial plot of single-grain AFT ages (Figure 4C) shows a significant number of grains are younger than the depositional age and few grains are older, evidencing a moderate partial reset of the AFT ages. For the samples MG7, MG9 and MG17, the central AFT ages are fairly younger than the depositional age whereas the sample MG20 is somewhat older (Table 1; Figure 4A). However, taking into account the uncertainty for these values (Figure 4A), the overall picture shows AFT ages quite similar to the depositional ages. Noticeable also, most of the apatite grains in the samples are euhedral. Therefore, the apatite crystals may be considered as mainly volcanic, which is consistent with the significant volcanic record evidences in the Chubut Group and related to coeval arc volcanism (Foix *et al.*, 2020). Then, the apatite grains have been moderately affected by a thermal event as evidenced by the modest partial reset of the AFT data.

### 4.2. Totally reset AHe ages

AHe samples yield single grain ages between  $15.9 \pm 1.3$  Ma and  $28.7 \pm 2.3$  Ma with low effective Uranium (eU) content that ranges from 5 to 40 ppm and relatively high Th/U ratio (5 to 12) (Table 2). The AHe ages are significantly younger than the depositional age (Figure 4A) and indicate a post-depositional resetting. Although no correlation appears between AHe

dates and eU content, correlation is recognized to some extent between AHe dates and sphere equivalent radius  $R_s$  size (Figure 4B), which means that the cooling occurred at moderate rates.

### 4.3. Thermal history

With the aim of evaluating the thermal history of the San Bernardo FTB, time-temperature (T-t) histories for samples MG7, MG17 and MG20 have been realized through inverse modeling with the QTQt software (v. 5.7.1; Gallagher, 2012). The QTQt software allows inverting AFT annealing and AHe diffusion parameters with the Markov Chain Monte Carlo method (Gallagher *et al.*, 2009; Gallagher, 2012) for single samples. He diffusion model incorporating the impact of radiation damage in apatite from Flowers *et al.* (2009), rather than the He diffusion model from Gautheron *et al.* (2009), has been used because of the relatively low eU content and thus damage content. Beyond the He diffusion model, AFT annealing kinetic model by Ketcham *et al.* (2007) has been considered. The modeling procedure is detailed in Gallagher (2012). The input parameters used to model each sample are the single-grain AFT and AHe ages, as well as the grains sizes and the chemical characteristics for AHe data. Main constraints were the depositional age of each sample (at  $20 \pm 10^\circ\text{C}$ ) and a present-day temperature at  $10 \pm 10^\circ\text{C}$ . A high-temperature constraint has been added closely before the deposition age as the high Th/U ratio (Table 2) suggests a volcanic origin for those apatite crystals, meaning that these crystals have been formed a short time before their deposition. This supposedly volcanic origin is also consistent with the euhedral shape of most of the apatite grains (not recycled). The thermal history results (Figure 5) are strongly impacted by the total reset of the AHe data that impose a minimum temperature of  $\sim 60^\circ\text{C}$  between 35 and 18 Ma. Therefore, the models for the samples MG17 and MG20 suggest the presence of a significant heating phase ( $> 60^\circ\text{C}$ ) through the late Oligocene to the early Miocene, closely

followed by a cooling event starting from the early Miocene (Figure 5). However, the model obtained for the sample MG7 indicates a prior heating event that may have started during the Eocene, and a subsequent slow cooling through the Oligocene, which seems to have accelerated during the early Miocene (Figure 5). On the other hand, given the AHe ages dispersion for the sample MG7 and the absence of fission track lengths, the modeling may be not precise enough to define precisely the onset of cooling. However, predicted values obtained for AHe and AFT ages are mostly consistent with observed ages (Figure 5), meaning that the model is valuable

#### 4.4. K-Ar ages

The tilted basalt and the basaltic dike yield ages of  $23.71 \pm 0.34$  and  $2.84 \pm 0.04$  Ma, respectively. Age results are given at the  $1\sigma$  confidence level and details are given in Table 3. These ages are in agreement with former studies, which reported ages between 28 and 18 Ma for the Buen Pasto basalts and younger than 4 Ma for Cerro Grande basalts (Sinito, 1980; Linares *et al.*, 1989; Bruni *et al.*, 2008). Thus, our results further support earlier observations that the area was affected by at least two intraplate volcanic events from the late Oligocene to the early Miocene, and later, through the Pliocene. Overall, the Oligo-Miocene Buen Pasto basalts display ages between 28 and 18 Ma, but only ages older than 20.5 Ma have been previously reported (Bruni *et al.*, 2008) close to the samples. The youngest K-Ar ages ( $< 20$  Ma) have been obtained about 20 km to the north and to the east of our study area (Bruni *et al.*, 2008). As the erosion of this Oligo-Miocene basaltic cover can be inferred from the isolated and remnants basaltic plateaus (see cross-sections on Figure 1C), the upper layers of the basaltic cover with ages younger than 20 Ma may have been removed or altered. Then, as demonstrated by the tilting of the Oligo-Miocene sampled basalt, the flat Pliocene basalts and

the K-Ar ages obtained here, a tectonic phase occurred between the deposition of these Oligo-Miocene and Pliocene basaltic layers.

## 5. Discussion

Consistent totally reset Oligo-Miocene AHe ages and partially reset AFT ages have been obtained in all the samples. Thermal models (Figure 5) are coherent with a debatable period of heating phase between the Cretaceous and the Eocene. This period is followed by a significant heating event from the Eocene to the early Miocene with peak temperatures reached at ca.  $30 \pm 5$  Ma, roughly coincident with the K-Ar ages obtained in the area for the Buen Pasto basalts (Figure 1A) and the proposed age of the San Bernardo Complex (Pezzuchi and Fernández, 2001; Pezzuchi, 2018). Thermal models show that a maximum temperature of 60 – 80°C was reached at 20 – 35 Ma, which can be explained by either a sedimentary load, basaltic load and / or magmatic heating effects. We will also discuss the tectonic implications in the post-heating phase recorded into the San Bernardo FTB through the Miocene.

### 5.1. Burial heating below sediments

Deposition of the Chubut deposits in the southwestern San Bernardo FTB is directly controlled by fault activity and the development of folds (Gianni *et al.*, 2015). Seismic data show that synorogenic Cretaceous deposits were buried below few hundred meters of Paleogene deposits, especially between anticlines (Rio Chico Formation; Gianni *et al.*, 2015), a rock column that is not sufficient to reset the low-temperature thermochronometers, not even the AHe one. In areas where no Paleogene deposits have been recognized, Oligo-Miocene basalts (Buen Pasto Formation) lie directly on top of the Chubut Group strata

(Gianni *et al.*, 2015; Navarrete *et al.*, 2015; Navarrete *et al.*, 2016; Allard *et al.*, 2020). This unconformity indicates that underlying formations were at the surface prior the emplacement of these basalts. This is inconsistent with a significant burial below a Paleogene cover. Although the removal of Paleogene sediments cannot be ruled out, the lack of significant Paleogene sedimentary burial is roughly supported by the thermal models which show a period of relatively slow heating between the Cretaceous and the Eocene (Figure 5) that can be related to a gradual sedimentary burial.

Thus, considering that approximately 2 km of sediments are necessary to reset totally the AHe (with a closure temperature of  $\sim 65^{\circ}\text{C}$ ; e.g., Flowers *et al.*, 2009; Gautheron *et al.*, 2009) and partially the AFT thermochronometers, using an average geothermal gradient of  $30^{\circ}\text{C}/\text{km}$  (according to Ávila and Dávila, 2018; Vieira and Hamza, 2019), and without volcanic impact, we exclude sedimentary burial as main cause for heating.

### *5.2. Impact of the Cenozoic intraplate volcanic activity*

Thermal models show that maximum temperature of  $60 - 80^{\circ}\text{C}$  was reached at  $20 - 35$  Ma, which is roughly coeval with the emplacement of the Eocene San Bernardo Complex and the Oligo-Miocene Buen Pasto basalts (Figures 2A, 2B and 3). This 15 m.y. heating event recorded by all the samples may indicate the occurrence of a large thermal event in the southwestern San Bernardo FTB, that cannot be restricted to some local lava flow deposits. Indeed, instantaneous heating events near the surface are associated to local downward thermal heating below the basalts (Fayon and Whitney, 2007; Hu *et al.*, 2020). For example, with a basaltic flood thick of 50 m and a temperature of  $1000^{\circ}\text{C}$ , heating may affect instantly the first 250 meters of rocks beneath the basalts (Fayon and Whitney, 2007), that may in turn affect low-temperature thermochronometers in near-surface rocks (Hu *et al.*, 2020), but not a

large area around or rocks at greater depth. The Pliocene Cerro Grande basalts are a reliable evidence that downward heating below the basalts does not result in regional heating processes. Although the Pliocene intraplate volcanism was less extended and less significant than the widespread Oligo-Miocene volcanism (Bruni et al., 2008), no Pliocene thermal perturbation has been evidenced by our data, even in the sample MG9 collected at less than one kilometer of the Pliocene basalts (Figures 1A and 1D). In other words, the intraplate Pliocene volcanic event did not trigger any significant heating by downward thermal diffusion able to reset the AHe age of the sample MG9 (Figure 6D). Thus, we consider that if the downward heating below the Oligo-Miocene basalts heated surely near-surface rocks during their emplacement, it may have not directly affected the samples located at greater depth at this time and therefore not subjected to the impact of downward heating.

Given the absence of a significant Cenozoic sedimentary burial in the area and the superficial impact of basalts emplacement, we propose that the heating phase observed is most likely related to the combination of a modest burial exerted by the volcanic deposits associated with a significant increase of the geothermal gradient due to a long-term heat flow anomaly in the entire area. Although there is an absence of constraint about the thickness of the original basaltic cover (and hence of its erosion; Figures 1A and 1C), a modest burial of the Cretaceous strata produced by the basaltic cover cannot be ignored as the Oligo-Miocene intraplate volcanism lasted for at least ~10 Ma and covered vast areas of the foreland.

Considering an average geothermal gradient of ~30 °C/km after the cessation of the volcanic activity at ~18 Ma, and a closure temperature of ~65°C for the AHe system for low eU content (e.g. Gautheron et al., 2009), a basaltic cover thickness of at least one kilometer above the entire San Bernardo FTB would have been necessary to maintain sufficient temperatures (> 65 °C) later than 18 Ma and recorded the younger AHe ages. Then, a comparable erosion of the basaltic cover would have been required in order to achieve current basalt thicknesses.



Even a modest erosion may have been sufficient to erode intensively the Oligo-Miocene basalts of the Buen Pasto Formation as these silicate rocks is easily weathered (Meybeck, 1987; Margirier *et al.*, 2019), especially during a climatic optimum, here through the late middle Miocene (Zachos *et al.*, 2001). Nevertheless, the scenario involving a thick basaltic cover thickness of at least one kilometer is not suitable with: 1) the thickness of the basaltic layers in the whole central Patagonia as they often display only tens of meters (Figure 1D; up to 100-200m locally according to Bruni, 2007), and 2) the geological record as the Neogene sedimentary units in surrounding depocenters which do not show any significant basalt sourcing (Anselmi *et al.*, 2004; Sciutto *et al.*, 2008; Pezzuchi, 2018) and are subjected to felsic sources coming from the main Cordillera (Genge, 2021).

Considering those arguments, a basaltic cover thickness of few hundred meters alone was not sufficient to maintain high temperatures in the sediments below. Indeed, cooling may have occurred instantly at the end of the volcanic event estimated at ~18 Ma according to the K-Ar ages obtained on the Oligo-Miocene basaltic cover across the San Bernardo FTB (this work; Sinito, 1980; Linares *et al.*, 1989; Bruni *et al.*, 2008), while few AHe ages are younger than 18 Ma and models evidence a moderate cooling instead of a very fast cooling. We thus propose that the younger AHe ages obtained are related to the persistence of the volcanic activity up to ~16 Ma. As a portion of the basaltic cover has been eroded on top, the timing of the cessation of the volcanic activity so far defined at ~18 Ma, which corresponds actually to the youngest age obtained by K-Ar dating across the San Bernardo FTB (Bruni *et al.*, 2008), may have been underestimated as the topmost basaltic layers have been removed.

It is noteworthy that the Eocene and Oligo-Miocene volcanic products were extruded through several extensional faults and fissures (Gianni *et al.*, 2017) and accompanied by the emplacement of sills and dikes over the San Bernardo FTB (Pezzuchi and Fernández, 2001; Plazibat *et al.*, 2019) that caused the entire area to be affected by a high heat flow that

increases the geothermal gradient in this area from the Eocene to early Miocene. This anomalous high heat flow in the southwestern San Bernardo FTB may have contributed to maintaining high temperatures even after the cessation of the volcanic activity defined at ~18 Ma (Bruni *et al.*, 2008) or possibly persisting to at least 16 Ma. Thus, the differences observed between each model may result from the variations of the geothermal gradient through time and space. For example, considering the location of the sample MG7 (directly west of the Lago Musters), a higher heat flow during the Eocene in this area due to the emplacement of the San Bernardo Complex may explain the earlier heating phase observed (Figures 5 and 6A).

In the light of these elements, we proposed a schematic reconstruction of the area, focused on a transect including samples MG9, MG7 and MG17 and considered as representative of the whole area (Figure 6). At Eocene time, the samples were at a different position at depth in the Cretaceous sediments, and the first Eocene volcanism period started to modify the thermal gradient (Figure 6A). As soon as the late Oligocene, basaltic layers covered the whole area, somewhat burying the samples, and the thermal gradient increased due to the emplacement of sills, dikes and the effects of the downward thermal diffusion from the surface (Figure 6B) that possibly affected samples located near the surface. The thermal gradient is maintained in the whole area due to the continuous volcanic activity from the late Oligocene to the early Miocene. Then, the samples may have cooled down slowly when the thermal gradient decreased to the current average value of ~30°C/km (Ávila and Dávila, 2018; Vieira and Hamza, 2019) at the end of this prolonged intraplate volcanic phase (Figure 6C).

### *5.3. The Miocene deformation phase*

As suggested in the previous sections, a cooling episode from c. 20 Ma to present is then observed, at the end of the Oligo-Miocene intraplate volcanic event. The thermal models (Figure 5), indicate that the samples cooled down at moderate rates, with a maximum cooling rate of  $\sim 4^{\circ}\text{C}/\text{Ma}$ , for the sample MG20, considering a peak temperature of  $80^{\circ}\text{C}$  at ca. 20 Ma (Figure 5). For the sample MG20, cooling occurred instantly at the presumed end of the magmatic episode ( $\sim 18$  Ma), which is consistent with the cessation of the volcanic event. Nevertheless, the obtained cooling rate is not compatible with a post-magmatic cooling, which is usually much faster.

Giving the ages obtained by K-Ar dating on the tilted basalt and the undeformed basalt,  $23.71 \pm 0.34$  and  $2.84 \pm 0.04$  Ma, respectively, deformation phase occurred between the early Miocene and Pliocene. Growth strata observed in surrounding sedimentary records and reactivation of inherited normal faults pointed to the existence of a tectonic event during the middle Miocene in the study area (e.g. Gianni *et al.*, 2017), which, according to Maloney *et al.* (2013), could be related to the change of convergence of the Nazca plate. This deformation event was also evidenced in the northern (Gastre Basin; Bilmes *et al.*, 2013) and the southern Patagonian Broken Foreland (Deseado Massif; Giacosa *et al.*, 2010), although low-temperature in-situ thermochronology studies in these areas suggest minor vertical displacements during the Neogene as they evidence a lack of thermochronology signal since the Paleogene (Savignano *et al.*, 2016; Fernández *et al.*, 2020; Genge *et al.*, 2021). Indeed, the latter thermochronology data and associated thermal modeling characterize a slow cooling of the whole foreland since the Late Cretaceous, with the lack of any particular thermal event. Nevertheless, few AHe ages from local areas of the northern Patagonian Broken Foreland record younger Neogene ages and have been related to the close and coeval intraplate volcanic activity (Savignano *et al.*, 2016; Genge *et al.*, 2021), as we suppose it is the case along the San Bernardo FTB. We thus conclude that, as previously proposed for other parts of

the Patagonian Broken Foreland (Savignano *et al.*, 2016; Fernández *et al.*, 2020; Genge *et al.*, 2021), the main deformation of the southern San Bernardo FTB occurred from the Cretaceous to the early Paleogene, while the middle-late Miocene deformation was modest (Figure 6C), especially in terms of vertical displacements.

Besides this modest deformation episode related to the Andean growth, a generalized uplift of the continental plate that affected distal areas may have started in the middle-late Miocene. Guillaume *et al.* (2009) propose dynamic topography associated with the subduction of ridge segments as the main cause for this modest-amplitude and large-wavelength uplift of the foreland. Thus, according to these authors, the San Bernardo FTB may have experienced a constant and moderate tilting to the north since the middle-late Miocene. Nevertheless, taking into account the AFT data, which are not able to detect minor vertical movements, and thermal modeling obtained south of the study area into the Deseado Massif (Fernández *et al.*, 2020), the dynamic topography in the central Patagonian foreland may have minor effects on the low-temperature thermochronometers as no particular accelerated cooling events have been evidenced during the Miocene. Furthermore, the preservation of fluvial terraces around the San Bernardo FTB demonstrates that low erosion affected the study region, possibly related to climatic changes since the late Miocene (Guillaume *et al.*, 2009). Thus, minor regional uplift of less than 300-200 meters related to dynamic topography (Ávila and Dávila, 2020) and associated with the increased aridity of the Patagonian foreland from the late Miocene and consequent low erosion rates (Blisniuk *et al.*, 2005), do not allow a significant exhumation of the rocks in this area.

Considering field observations indicating a modest deformation (see new bedding attitudes reported on Figure 1A), basalts weathering stated above, and thermochronology results in surrounding areas (Savignano *et al.*, 2016; Fernández *et al.*, 2020; Genge *et al.*, 2021), it is proposed here that the role of tectonism, dynamic topography and erosion during the Miocene

is also limited along the southwestern San Bernardo FTB but may have triggered a modest exhumation of the samples from early Miocene to present (Figure 6C). We can estimate this exhumation of ~1 km at most. Associated with the slow decrease of the geothermal gradient following the cessation of magmatic activity, this moderate exhumation may have been responsible for the moderate cooling evidenced on the models.

## **6. Conclusions**

AFT and AHe thermochronology have been applied for the first time to the San Bernardo FTB to constrain the tectono-thermal evolution of this intraplate belt. The main results from dating and thermal modeling highlight a period of slow heating from the Cretaceous to the Eocene, related with moderate sedimentary burial. According to the thermal models, the ages of the Buen Pasto basalts and San Bernardo Complex rocks, the following Eocene – early Miocene heating phase recorded by our data must be regarded as a magmatic signal. Indeed, we consider that the long-term intraplate magmatism phase, which started during the Eocene and continued actively to the early Miocene, may be related to moderate burial of the studied samples below the basaltic cover associated with a significant increase of the geothermal gradient in the area. The emplacement of dikes and sills, the circulation of hot fluids along faults and fissures, and the downward heating below the basalts at the surface may have contributed to maintaining a higher geothermal gradient in the entire area to the early Miocene. Then, the post-heating phase most likely resulted from the cessation of this long-term volcanic activity and the subsequent decrease of the geothermal gradient to average values, probably combined with a modest exhumation (< 1 km), which has been triggered by the middle-late Miocene tectonic activity, dynamic topography and erosion processes.

## 7. Acknowledgements

This work was funded by the University of Padova (Progetto di Ateneo 2015, CPDA158355), the Tellus Program of CNRS/ INSU and the CESSUR Program of CNRS / INSU for the AHe analysis. A. Hildenbrand is kindly thanked for K-Ar analysis (Orsay, France). Thanks to R. Pinna-Jamme and F. Haurine for their technical support in AHe analysis. V. Olivetti (University of Padua) and M. Marquez (SEGEMAR, Comodoro Rivadavia) are thanked for their constructive comments.

## References

- Allard, J.O., Foix, N., Buetti, S.A., Sánchez, F.M., Ferreira, M.L. and Atencio, M., 2020. Comparative structural analysis of inverted structures in the San Bernardo fold belt (Golfo San Jorge basin, Argentina): Inversion controls and tectono-sedimentary context of the Chubut Group: *Journal of South American Earth Sciences*, **97**, p. 102405.
- Anselmi, G., Panza, J.L.A., Cortés, J.M. and Ragona, D., 2004. *Hoja Geológica 4569-II El Sombrero*: Servicio Geológico Minero Argentino. Instituto de Geología y Recursos Minerales, Servicio Geológico Minero Argentino. Boletín 271, 70p. Buenos Aires.
- Ault, A.K., Gautheron, C. and King, G.E., 2019. Innovations in (U–Th)/He, fission track, and trapped charge thermochronometry with applications to earthquakes, weathering, surface-mantle connections, and the growth and decay of mountains: *Tectonics*, **38**, p. 3705–3739.
- Ávila, P., & Dávila, F. M. (2018). Heat flow and lithospheric thickness analysis in the Patagonian asthenospheric windows, southern South America. *Tectonophysics*, **747**, 99-107.
- Ávila, P., & Dávila, F. M. (2020). Lithospheric thinning and dynamic uplift effects during slab window formation, southern Patagonia (45°-55° S). *Journal of Geodynamics*, **133**, 101689.
- Bablon, M., Quidelleur, X., Samaniego, P., Le Pennec, J.-L., Lahitte, P., Liorzou, C., Bustillos, J.E. and Hidalgo, S., 2018. Eruptive chronology of Tungurahua volcano (Ecuador) revisited based on new K-Ar ages and geomorphological reconstructions: *Journal of Volcanology and Geothermal Research*, **357**, p. 378–398.
- Barcat, C., Cortiñas, J.S., Nevistic, V.A. and Zucchi, H.E., 1989. Cuenca Golfo San Jorge: *Cuencas Sedimentarias Argentinas*, **6**, p. 319–345.
- Barreda, V. and Bellosi, E., 2014. Ecosistemas terrestres del Mioceno Temprano de la Patagonia central, Argentina: primeros avances: *Revista del Museo Argentino de Ciencias Naturales nueva serie*, **5**, p. 125–134.
- Bellosi, E.S., 2010. Loessic and fluvial sedimentation in Sarmiento Formation pyroclastics, middle Cenozoic of central Patagonia. In: *The Paleontology of Gran Barranca*:

- Evolution and Environmental Change through the Middle Cenozoic of Patagonia*. Cambridge University Press, Cambridge, p. 278–292.
- Bilmes, A., D’Elia, L., Franzese, J.R., Veiga, G.D. and Hernández, M., 2013. Miocene block uplift and basin formation in the Patagonian foreland: the Gastre Basin, Argentina: *Tectonophysics*, **601**, p. 98–111.
- Blackstone, D.L., 1980. Foreland deformation; compression as a cause: *Rocky Mountain Geology*, **18**, p. 83–100.
- Blisniuk, P. M., Stern, L. A., Chamberlain, C. P., Idleman, B., & Zeitler, P. K. (2005). Climatic and ecologic changes during Miocene surface uplift in the Southern Patagonian Andes. *Earth and Planetary Science Letters*, **230**(1-2), 125-142.
- Brandon, M.T., Roden-Tice, M.K. and Garver, J.I., 1998. Late Cenozoic exhumation of the Cascadia accretionary wedge in the Olympic Mountains, northwest Washington State: *Geological Society of America Bulletin*, **110**, p. 985–1009.
- Bruni, S., D’ORAZIO, M., Haller, M.J., Innocenti, F., Manetti, P., PECskay, Z. and Tonarini, S., 2008. Time-evolution of magma sources in a continental back-arc setting: the Cenozoic basalts from Sierra de San Bernardo (Patagonia, Chubut, Argentina): *Geological Magazine*, **145**, p. 714–732.
- Bruni, S. (2007). The Cenozoic back-arc magmatism of Central Patagonia (44-46 S): activation of different mantle domains in space and time. Ph.D. thesis.
- Calk, L.C. and Naeser, C.W., 1973. The thermal effect of a basalt intrusion on fission tracks in quartz monzonite: *The Journal of Geology*, **81**, p. 189–198.
- Carignano, A.P., Paredes, J.M., Olazábal, S.X. and Valle, M.N., 2017. Ostracoda (Crustacea) from the Pozo D-129 formation (upper Barremian?–Aptian), Golfo san Jorge basin, Patagonia, Argentina: taxonomic descriptions, palaeoenvironments and palaeogeographical implications: *Cretaceous Research*, **78**, p. 206–220.
- Casal, G.A., Allard, J.O. and Foix, N., 2015. Análisis estratigráfico y paleontológico del Cretácico Superior en la Cuenca del Golfo San Jorge: nueva unidad litoestratigráfica para el Grupo Chubut: *Revista de la Asociación Geológica Argentina*, **72**, p. 77–95.
- Cavazza, W., Albino, I., Galoyan, G., Zattin, M. and Catto, S., 2019. Continental accretion and incremental deformation in the thermochronologic evolution of the Lesser Caucasus: *Geoscience Frontiers*, **10**, p. 2189–2202.
- Davis, G.A., Cong, W., Yadong, Z., Jinjiang, Z., Changhou, Z. and Gehrels, G.E., 1998. The enigmatic Yinshan fold-and-thrust belt of northern China: New views on its intraplate contractional styles: *Geology*, **26**, p. 43–46.
- Dunkl, I., 2002. TRACKKEY: a Windows program for calculation and graphical presentation of fission track data: *Computers & Geosciences*, **28**, p. 3–12.
- Echaurren, A., Folguera, A., Gianni, G., Orts, D., Tassara, A., Encinas, A., Giménez, M. and Valencia, V., 2016. Tectonic evolution of the North Patagonian Andes (41–44 S) through recognition of syntectonic strata: *Tectonophysics*, **677**, p. 99–114.
- Ehlers, T.A., Armstrong, P.A. and Chapman, D.S., 2001. Normal fault thermal regimes and the interpretation of low-temperature thermochronometers: *Physics of the Earth and Planetary Interiors*, **126**, p. 179–194.
- Encinas, A., Folguera, A., Bechis, F., Finger, K.L., Zambrano, P., Pérez, F., Bernabé, P., Tapia, F., Rizzo, R. and Buatois, L., 2018. The late Oligocene–early Miocene marine transgression of Patagonia. In: *The Evolution of the Chilean-Argentinean Andes* Springer, p. 443–474.
- Fayon, A.K. and Whitney, D.L., 2007. Interpretation of tectonic versus magmatic processes for resetting apatite fission track ages in the Niğde Massif, Turkey: *Tectonophysics*, **434**, p. 1–13.

- Fernández, M.L., Mazzoli, S., Zattin, M., Savignano, E., Genge, M.C., Tavani, S., Garrone, A. and Franchini, M., 2020. Structural controls on Jurassic gold mineralization, and Cretaceous-Tertiary exhumation in the foreland of the southern Patagonian Andes: New constraints from La Paloma area, Deseado Massif, Argentina: *Tectonophysics*, **775**, p. 228302.
- Figari, C.E., Scasso, R.A., Cúneo, N.R. and Escapa, I.H., 2016. Estratigrafía y evolución geológica de la Cuenca de Cañadón Asfalto, Provincia del Chubut, Argentina. *Lat. Am. J. Sedimentol. Basin Anal.*, **22** (2) (2015), pp. 135-169
- Flowers, R.M., Ketcham, R.A., Shuster, D.L. and Farley, K.A., 2009. Apatite (U–Th)/He thermochronometry using a radiation damage accumulation and annealing model: *Geochimica et Cosmochimica acta*, **73**, p. 2347–2365.
- Foix, N., Allard, J.O., Ferreira, M.L. and Atencio, M., 2020. Spatio-temporal variations in the Mesozoic sedimentary record, Golfo San Jorge Basin (Patagonia, Argentina): Andean vs. cratonic sources: *Journal of South American Earth Sciences*, **98**, p. 102464.
- Foix, N., Paredes, J.M. and Giacosa, R.E., 2013. Fluvial architecture variations linked to changes in accommodation space: Río Chico Formation (late Paleocene), Golfo San Jorge basin, Argentina: *Sedimentary Geology*, **294**, p. 342–355.
- Galbraith, R.F. and Laslett, G.M., 1993. Statistical models for mixed fission track ages: *Nuclear tracks and radiation measurements*, **21**, p. 459–470.
- Gallagher, K., 2012. Transdimensional inverse thermal history modeling for quantitative thermochronology: *Journal of Geophysical Research: Solid Earth*, **117**, B02408
- Gallagher, K., Charvin, K., Nielsen, S., Sambridge, M. and Stephenson, J., 2009. Markov chain Monte Carlo (MCMC) sampling methods to determine optimal models, model resolution and model choice for Earth Science problems: *Marine and Petroleum Geology*, **26**, p. 525–535.
- Gautheron, C. and Tassan-Got, L., 2010. A Monte Carlo approach to diffusion applied to noble gas/helium thermochronology: *Chemical Geology*, **273**, p. 212–224.
- Gautheron, C., Tassan-Got, L., Barbarand, J. and Pagel, M., 2009. Effect of alpha-damage annealing on apatite (U–Th)/He thermochronology: *Chemical Geology*, **266**, p. 157–170.
- Genge, M. C., 2021. Tectonic evolution of the north-central Patagonia: a thermochronological approach. Ph.D. thesis.
- Genge, M. C., Zattin, M., Savignano, E., Franchini, M., Gautheron, C., Ramos, V. A. and Mazzoli S. (*In press*). The role of slab geometry in the exhumation of cordilleran-type orogens and their forelands: Insights from northern Patagonia. <https://doi.org/10.1130/B35767.1>
- Genise, J.F., Melchor, R.N., Bellosi, E.S., González, M.G. and Krause, M., 2007. New insect pupation chambers (Pupichnia) from the Upper Cretaceous of Patagonia, Argentina: *Cretaceous Research*, **28**, p. 545–559.
- Giacosa, R., Zubia, M., Sánchez, M. and Allard, J., 2010. Meso-Cenozoic tectonics of the southern Patagonian foreland: Structural evolution and implications for Au–Ag veins in the eastern Deseado Region (Santa Cruz, Argentina): *Journal of South American Earth Sciences*, **30**, p. 134–150.
- Gianni, G.M., Echaurren, A., Folguera, A., Likerman, J., Encinas, A., Garcia, H.P.A., Dal Molin, C. and Valencia, V.A., 2017. Cenozoic intraplate tectonics in Central Patagonia: Record of main Andean phases in a weak upper plate: *Tectonophysics*, **721**, p. 151–166.
- Gianni, G.M., Navarrete, C., Orts, D., Tobal, J., Folguera, A. and Giménez, M., 2015. Patagonian broken foreland and related synorogenic rifting: The origin of the Chubut Group Basin: *Tectonophysics*, **649**, p. 81–99.



- Gillot, P.-Y., Hildenbrand, A., Lefèvre, J.-C. and Albore-Livadie, C., 2006. The K/Ar dating method: principle, analytical techniques, and application to Holocene volcanic eruptions in southern Italy. *Acta Vulcanologica*, **18**(2), 55–66.
- Gleadow, A.J.W., 1981. Fission-track dating methods: what are the real alternatives? *Nuclear Tracks*, **5**, p. 3–14.
- Green, P.F., Duddy, I.R., Laslett, G.M., Hegarty, K.A., Gleadow, A.W. and Lovering, J.F., 1989. Thermal annealing of fission tracks in apatite 4. Quantitative modelling techniques and extension to geological timescales: *Chemical Geology: Isotope Geoscience Section*, **79**, p. 155–182.
- Guillaume, B., Martinod, J., Husson, L., Roddaz, M., & Riquelme, R. (2009). Neogene uplift of central eastern Patagonia: Dynamic response to active spreading ridge subduction?. *Tectonics*, **28**(2).
- Guimerá, J. and Alvaro, M., 1990. Structure et évolution de la compression alpine dans la Chaîne Ibérique et la Chaîne côtière catalane (Espagne): *Bulletin de la Société géologique de France*, **6**, p. 339–348.
- Guimerà Rosso, J.J., 2018. Structure of an intraplate fold-and-thrust belt: The Iberian Chain. A synthesis.: *Geologica acta*, **16**, p. 0427–438.
- Hechem, J.J., Homoc, J.F. and Figari, E.G., 1990. Estratigrafía del Chubutiano (Cretácico) en la Sierra de San Bernardo, cuenca del Golfo San Jorge, Argentina. In: *11 Congreso Geológico Argentino* p. 173e176.
- Homoc, J.F., Conforto, G.A., Lafourcade, P.A. and Chelotti, L.A., 1995. Fold belt in the San Jorge Basin, Argentina: an example of tectonic inversion: *Geological Society, London, Special Publications*, **88**, p. 235–248.
- Hu, D., Tian, Y., Hu, J., Rao, S., Wang, Y., Zhang, C. and Hu, S., 2020. Thermal imprints of late Permian Emeishan basalt effusion: Evidence from zircon fission-track thermochronology: *Lithos*, **352**, p. 105224.
- Hurford, A.J. and Green, P.F., 1983. The zeta age calibration of fission-track dating: *Chemical Geology*, **41**, p. 285–317.
- Kay, S.M., Ardolino, A.A., Gorring, M.L. and Ramos, V.A., 2007. The Somuncura Large Igneous Province in Patagonia: interaction of a transient mantle thermal anomaly with a subducting slab: *Journal of Petrology*, **48**, p. 43–77.
- Ketcham, R.A., Carter, A., Donelick, R.A., Barbarand, J. and Hurford, A.J., 2007. Improved modeling of fission-track annealing in apatite: *American Mineralogist*, **92**, p. 799–810.
- Ketcham, R.A., Gautheron, C. and Tassan-Got, L., 2011. Accounting for long alpha-particle stopping distances in (U–Th–Sm)/He geochronology: Refinement of the baseline case: *Geochimica et Cosmochimica Acta*, **75**, p. 7779–7791.
- Legarreta, L. and Uliana, M.A., 1994. Asociaciones de fósiles y hiatos en el Supracretácico-Neógeno de Patagonia: una perspectiva estratigráfico-secuencial: *Ameghiniana*, **31**, p. 257–281.
- Lesta, P. and Ferello, R., 1972. Región extraandina de Chubut y norte de Santa Cruz: *Geología Regional Argentina*, **2**, p. 602–687.
- Lesta, P., Ferello, R. and Chebli, G., 1980. Chubut extraandino. In: *Simposio Geología Regional Argentina. Academia Nacional de Ciencias de Córdoba* p. 1307–1387.
- Lin, W., Faure, M., Chen, Y., Ji, W., Wang, F., Wu, L., Charles, N., Wang, J. and Wang, Q., 2013. Late Mesozoic compressional to extensional tectonics in the Yiwulüshan massif, NE China and its bearing on the evolution of the Yinshan–Yanshan orogenic belt: Part I: Structural analyses and geochronological constraints: *Gondwana Research*, **23**, p. 54–77.
- Linares, E., González, R.R. and Argentina, A.G., 1989. *Catálogo de edades radimétricas de la República Argentina, años 1957-1987*: Asociación Geológica Argentina.

- Maloney, K.T., Clarke, G.L., Klepeis, K.A. and Quevedo, L., 2013. The Late Jurassic to present evolution of the Andean margin: Drivers and the geological record: *Tectonics*, **32**, p. 1049–1065.
- Malusà, M.G., Polino, R., Zattin, M., Bigazzi, G., Martin, S. and Piana, F., 2005. Miocene to Present differential exhumation in the Western Alps: Insights from fission track thermochronology: *Tectonics*, **24**, p. TC3004.
- Margirier, A., Braun, J., Gautheron, C., Carcaillet, J., Schwartz, S., Jamme, R.P. and Stanley, J., 2019. Climate control on Early Cenozoic denudation of the Namibian margin as deduced from new thermochronological constraints: *Earth and Planetary Science Letters*, **527**, p. 115779.
- Meybeck, M., 1987. Global chemical weathering of surficial rocks estimated from river dissolved loads: *American journal of science*, **287**, p. 401–428.
- Navarrete, C., Gianni, G., Echaurren, A., Kingler, F.L. and Folguera, A., 2016. Episodic Jurassic to lower Cretaceous intraplate compression in Central Patagonia during Gondwana breakup: *Journal of Geodynamics*, **102**, p. 185–201.
- Navarrete, C.R., Gianni, G.M. and Folguera, A., 2015. Tectonic inversion events in the western San Jorge Gulf Basin from seismic, borehole and field data: *Journal of South American Earth Sciences*, **64**, p. 486–497.
- Paredes, J.M., Aguiar, M., Ansa, A., Giordano, S., Ledesma, M. and Tejada, S., 2018. Inherited discontinuities and fault kinematics of a multiphase, non-colinear extensional setting: Subsurface observations from the South Flank of the Golfo San Jorge basin, Patagonia: *Journal of South American Earth Sciences*, **81**, p. 87–107.
- Paredes, J.M., Foix, N., Piñol, F.C., Nillni, A., Allard, J.O. and Marquillas, R.A., 2007. Volcanic and climatic controls on fluvial style in a high-energy system: the Lower Cretaceous Matasiete Formation, Golfo San Jorge basin, Argentina: *Sedimentary Geology*, **202**, p. 96–123.
- Paredes, J.M., Plazibat, S., Crovetto, C., Stein, J., Cayo, E. and Schiuma, A., 2013. Fault kinematics and depocenter evolution of oil-bearing, continental successions of the Mina del Carmen Formation (Albian) in the Golfo San Jorge basin, Argentina: *Journal of South American Earth Sciences*, **46**, p. 63–79.
- Peroni, G.O., Hegedus, A.G., Cerdan, J., Legarreta, L., Uliana, M.A. and Laffitte, G., 1995. Hydrocarbon accumulation in an inverted segment of the Andean Foreland: San Bernardo belt, Central Patagonia. In: Tankard A.J., Suárez S., Welsink H.J. (Eds.) *Petroleum basins of South America. American Association of Petroleum Geologists Memoir*, **62**, pp. 403–419.
- Pezzuchi, H. y Fernández, M. I. 2001. Mapa de la Hoja Geológica 4569-III: Sarmiento, provincia del Chubut. Instituto de Geología y Recursos Minerales-SEGEMAR (inérita), Buenos Aires.
- Pezzuchi, H. D., 2018. Sarmiento. Hoja Geológica 4569-III. Programa Nacional de Cartas Geológicas de la República Argentina 1:250.000. Carta Geológica de la República Argentina. Boletín 318. Buenos Aires, Servicio Geológico Minero Argentino. Instituto de Geología y Recursos Minerales.
- Plazibat, S., Rasgido, A. and Paredes, J.M., 2019. Subsurface characterization of Cenozoic igneous activity at Cerro Dragón area (Golfo San Jorge Basin, central Patagonia): Implications for basin evolution and hydrocarbon prospectivity: *Journal of South American Earth Sciences*, **96**, p. 102389.
- Rapela, C.W. and Kay, S.M., 1988. Late Paleozoic to Recent magmatic evolution of northern Patagonia: *Episodes*, **11**, p. 175–182.
- Ré, G.H., Bellosi, E.S., Heizler, M., Vilas, J.F., Madden, R.H., Carlini, A.A., Kay, R.F. and Vucetich, M.G., 2010. A geochronology for the Sarmiento Formation at Gran

- Barranca. In: *The Paleontology of Gran Barranca: Evolution and Environmental Change through the Middle Cenozoic of Patagonia*. Cambridge University Press Cambridge, p. 46-60
- Remesal, M.B., Salani, F.M. and Cerredo, M.E., 2012. Petrología del complejo volcánico Barril Niyeu (Mioceno inferior), Patagonia Argentina: *Revista mexicana de ciencias geológicas*, **29**, p. 463–477.
- Roy, M., Kelley, S., Pazzaglia, F., Cather, S. and House, M., 2004. Middle Tertiary buoyancy modification and its relationship to rock exhumation, cooling, and subsequent extension at the eastern margin of the Colorado Plateau: *Geology*, **32**, p. 925–928.
- Samper, A., Quidelleur, X., Boudon, G., Le Friant, A. and Komorowski, J.C., 2008. Radiometric dating of three large volume flank collapses in the Lesser Antilles Arc: *Journal of Volcanology and Geothermal Research*, **176**, p. 485–492.
- Savignano, E., Mazzoli, S., Arce, M., Franchini, M., Gautheron, C., Paolini, M. and Zattin, M., 2016. (Un) Coupled thrust belt-foreland deformation in the northern Patagonian Andes: New insights from the Esquel-Gastre sector (41° 30'–43° S): *Tectonics*, **35**, p. 2636–2656.
- Sciutto, J.C., 1981. Geología del codo del río Senguerr, Chubut, Argentina. In: *CONGRESO GEOLÓGICO ARGENTINO*, Vol. **8**, No. 1981, p. 203–219.
- Sciutto, J.C., Césari, O., Lantanos, N. and Ardolino, A.A., 2008. Hoja Geológica 4569-IV Escalante, Provincia del Chubut. Servicio Geológico Minero Argentino. Instituto de Geología y Recursos Minerales, Boletín 351, 76 p.. Buenos Aires.
- Sharp, W.D., Renne, P.R., 2005. The  $^{40}\text{Ar}/^{39}\text{Ar}$  dating of core recovered by the Hawaii Scientific Drilling Project (phase 2), Hilo, Hawaii. *Geochemistry Geophysics Geosystems* **6**, Q04G17, doi:10.1029/2004GC000846. 18 pp.
- Sinito, A.M., 1980. Edades geológicas, radimétricas y magnéticas de algunas vulcanitas cenozoicas de las provincias de Santa Cruz y Chubut: *Rev. Asoc. Geol. Argent*, **35**, p. 332–339.
- Steiger, R.H. and Jäger, E., 1977. Subcommission on geochronology: convention on the use of decay constants in geo- and cosmochronology: *Earth and planetary science letters*, **36**, p. 359–362.
- Suarez, M., De La Cruz, R., Aguirre-Urreta, B. and Fanning, M., 2009. Relationship between volcanism and marine sedimentation in northern Austral (Aisén) Basin, central Patagonia: Stratigraphic, U–Pb SHRIMP and paleontologic evidence: *Journal of South American Earth Sciences*, **27**, p. 309–325.
- Tunik, M.A., Paredes, J.M., Fernández, M.I., Foix, N. and Allard, J.O., 2015. Análisis petrográfico de areniscas de la formación castillo (Albiano) en la faja plegada de San Bernardo, cuenca golfo San Jorge, Argentina. vol **72**, Revista de la Asociación Geológica Argentina, pp. 59-76
- Umazano, A.M., Bellosi, E.S., Visconti, G., Jalfin, G.A. and Melchor, R.N., 2009. Sedimentary record of a Late Cretaceous volcanic arc in central Patagonia: petrography, geochemistry and provenance of fluvial volcanoclastic deposits of the Bajo Barreal Formation, San Jorge Basin, Argentina: *Cretaceous Research*, **30**, p. 749–766.
- Vallati, P., Casal, G., Foix, N., Allard, J., Tomas, A.D.S. and Calo, M., 2016. First report of a Maastrichtian palynoflora from the Golfo san Jorge Basin, central Patagonia, Argentina: *Ameghiniana*, **53**, p. 495–505.
- Vermeesch, P., 2018. IsoplotR: A free and open toolbox for geochronology: *Geoscience Frontiers*, **9**, p. 1479–1493.

- Vieira, F., & Hamza, V. (2019). Assessment of Geothermal Resources of South America-A New Look. *International Journal of Terrestrial Heat Flow and Applied Geothermics*, **2**(1), 46-57.
- Willett, S.D., Fisher, D., Fuller, C., En-Chao, Y. and Chia-Yu, L., 2003. Erosion rates and orogenic-wedge kinematics in Taiwan inferred from fission-track thermochronometry: *Geology*, **31**, p. 945–948.
- Yonkee, W.A. and Weil, A.B., 2015. Tectonic evolution of the Sevier and Laramide belts within the North American Cordillera orogenic system: *Earth-Science Reviews*, **150**, p. 531–593.
- Zachos, J., Pagani, M., Sloan, L., Thomas, E. and Billups, K., 2001. Trends, rhythms, and aberrations in global climate 65 Ma to present: *science*, **292**, p. 686–693.

## Figure captions

Figure 1. (A) Geological map of the southern San Bernardo Fold-Thrust Belt showing K-Ar ages (<sup>1</sup>Sinito, 1980; <sup>2</sup>Linares *et al.*, 1989; <sup>3</sup>Bruni *et al.*, 2008; this study) on basalt units. Geological units from Pezzuchi (2018) and Sciutto *et al.* (2008). Principal structures from Homoc *et al.* (1995). (B) Stratigraphic log of the study area (modified after Allard *et al.*, 2020) with sampled formations; CG: Cerro Grande basalts, BP: Buen Pasto basalts, SBC: San Bernardo Complex. Cross-sections (C and D) inspired from new structural data, seismic analysis (Gianni *et al.*, 2015; Allard *et al.*, 2020) and existing cross-sections (Pezzuchi, 2018). Stratigraphic thickness of Chubut units on the cross-sections from Allard *et al.* (2020). Samples indicated on cross-sections correspond to projection of the location of sampling sites (15 kilometers maximum with sample MG7). Red squares correspond to places where pictures of tilted Oligo-Miocene Buen Pasto basalts (E) and Pliocene Cerro Grande basalts (F) have been taken.

Figure 2. Pictures of some apatite grains selected for (U-Th-Sm)/He dating from sample MG7 (A), MG17 (B) and MG20 (C) with dimensions of the grains.

Figure 3. Thin sections of dated samples MG18 (A) and MG21 (B) under cross-polarized light. Rocks are fine-grained basalts with olivine, pyroxene and plagioclase phenocrysts, and a groundmass composed of the same three minerals and interstitial glass. In order to remove heavier (olivine-pyroxene) and lighter (plagioclase) phenocrysts, only the groundmass was separated within density ranges of 2.94-3.06 and 2.93-3.04 for MG18 and MG21 samples, respectively. Such narrow and relatively heavy density selected ranges also allow us to eliminate weathered parts of the rock, if any. Green circles show the fractions kept for dating, while red cross show the fraction removed during mineral separation.

Figure 4. A. Comparison of apatite FT and (U-Th-Sm)/He ages with deposition ages for the samples collected in the Chubut Group. B. Diagrams representing AHe data ( $eU/AHe$  age,  $R_s/AHe$  age and depositional age /  $Th/U$ ). The effective Uranium content being  $eU=U+0.234\times Th+0.0046\times Sm$ . C. Radial plots with IsoplotR (Vermeesch, 2018) for single-grain AFT ages which evidence partial reset of the data.

Figure 5. Inverse modeling evidencing Eocene – early Miocene heating and cooling for all the samples which may have started at the end of the early Miocene. Each line represents the best-fit model (in bold) and the uncertainties. Dotted rectangles show the constraints used for the models as the deposition time (in bold) and the initial high temperatures. Below, thermal histories show the maximum likelihood model for each sample evidencing that models are poorly constrained between the Cretaceous and the Eocene. Then, observed vs predicted ages plots are shown for all the samples (inverse modeling data available upon request) and evidence that models are valuable.

Figure 6. Schematic sketches representative of the southwestern San Bernardo FTB evolution and including samples MG7, MG9 and MG17. The sketches evidence first the impact of modest Eocene (A) and significant Oligo-Miocene intraplate volcanism (B) on the geothermal gradient (e.g. moderate burial below the basaltic cover, downward thermal heating below the basalts, high heat flow circulation due to sills and dikes). Then the sketches show the probable combined effect of the slow decrease of the thermal gradient since the cessation of the volcanic activity combined with moderate exhumation (C) related to basalts weathering, deformation and dynamic topography. Finally, the absence of any effect of the last volcanic phase on the samples is illustrated on the sketch (D). AFT ages for each sample represented are in bold, AHe ages in italic and K-Ar ages in purple.

## **Table captions**

Table 1. Apatite fission tracks data for the samples collected in the Chubut Group including samples location, sampled formations sampled and stratigraphic ages.

Table 2. Apatite (U-Th-Sm)/He single-grain data results. AHe ages corrected using the ejection factor  $F_T$  (determined using the Monte Carlo simulation of Ketcham et al., 2011). Equivalent-sphere radius  $R_s$  calculated using procedure of Gautheron and Tassan-Got (2010). eU is the effective uranium concentration in ppm. Corrected ages given at  $1\sigma$  error.

Table 3. K-Ar dating results.

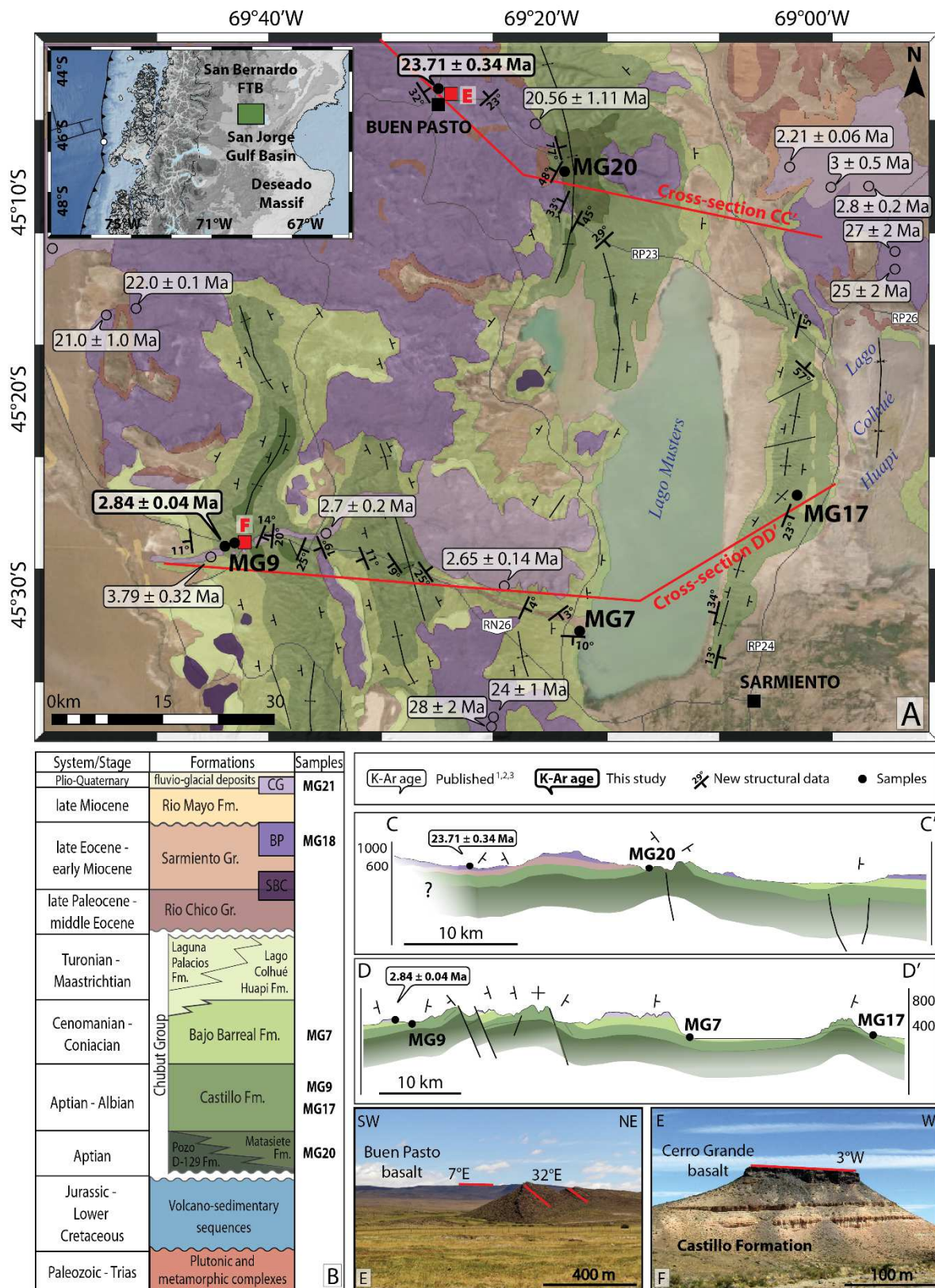


Figure 1.

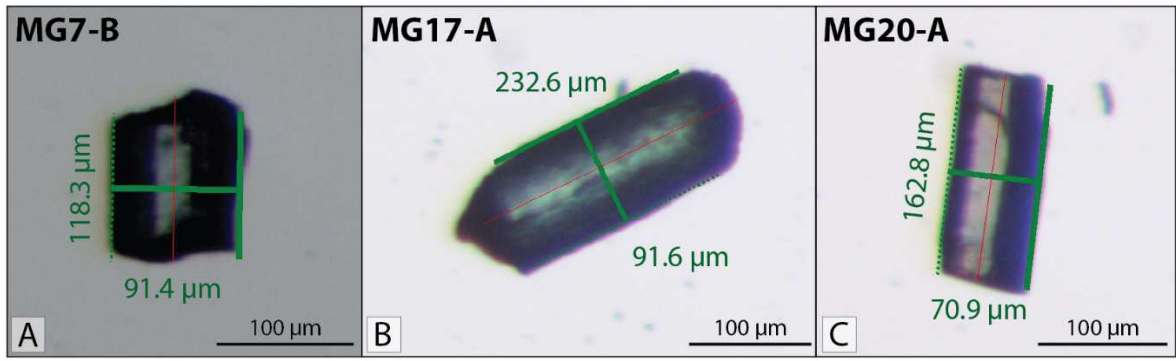


Figure 2.



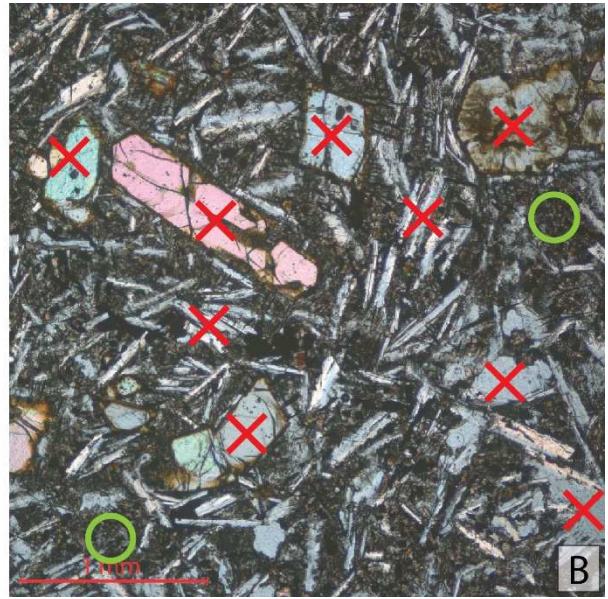
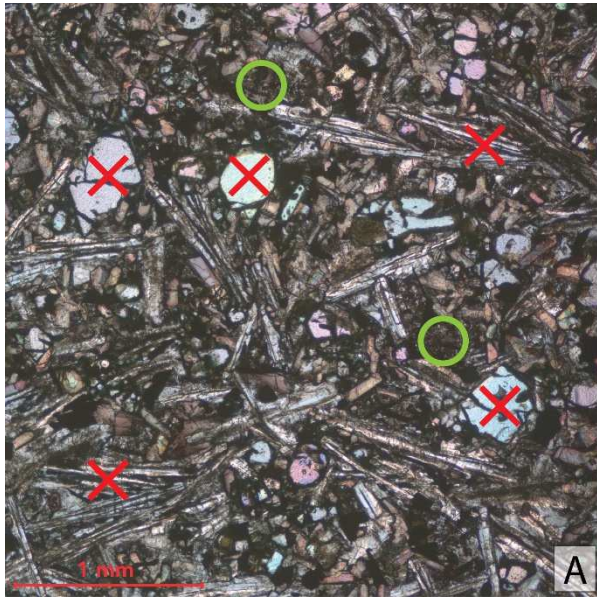


Figure 3.

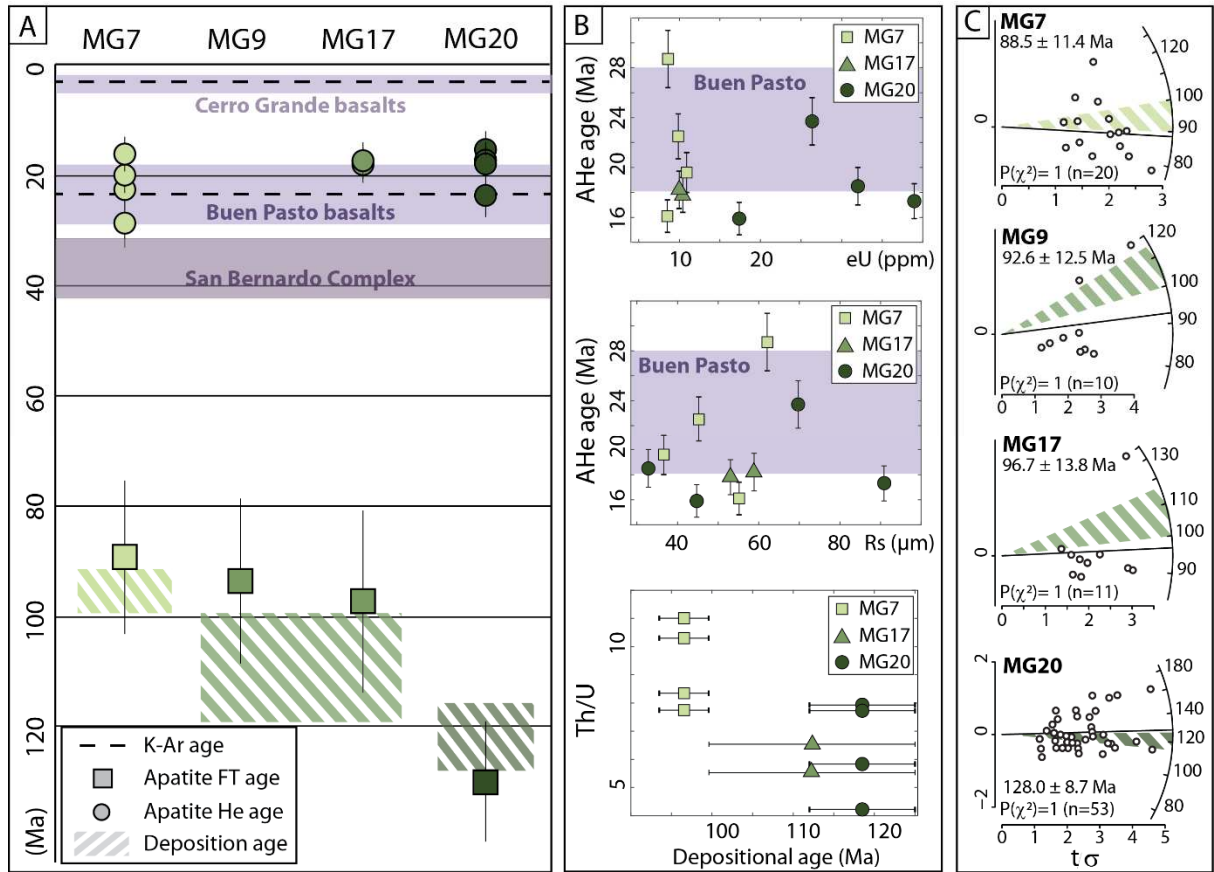


Figure 4.

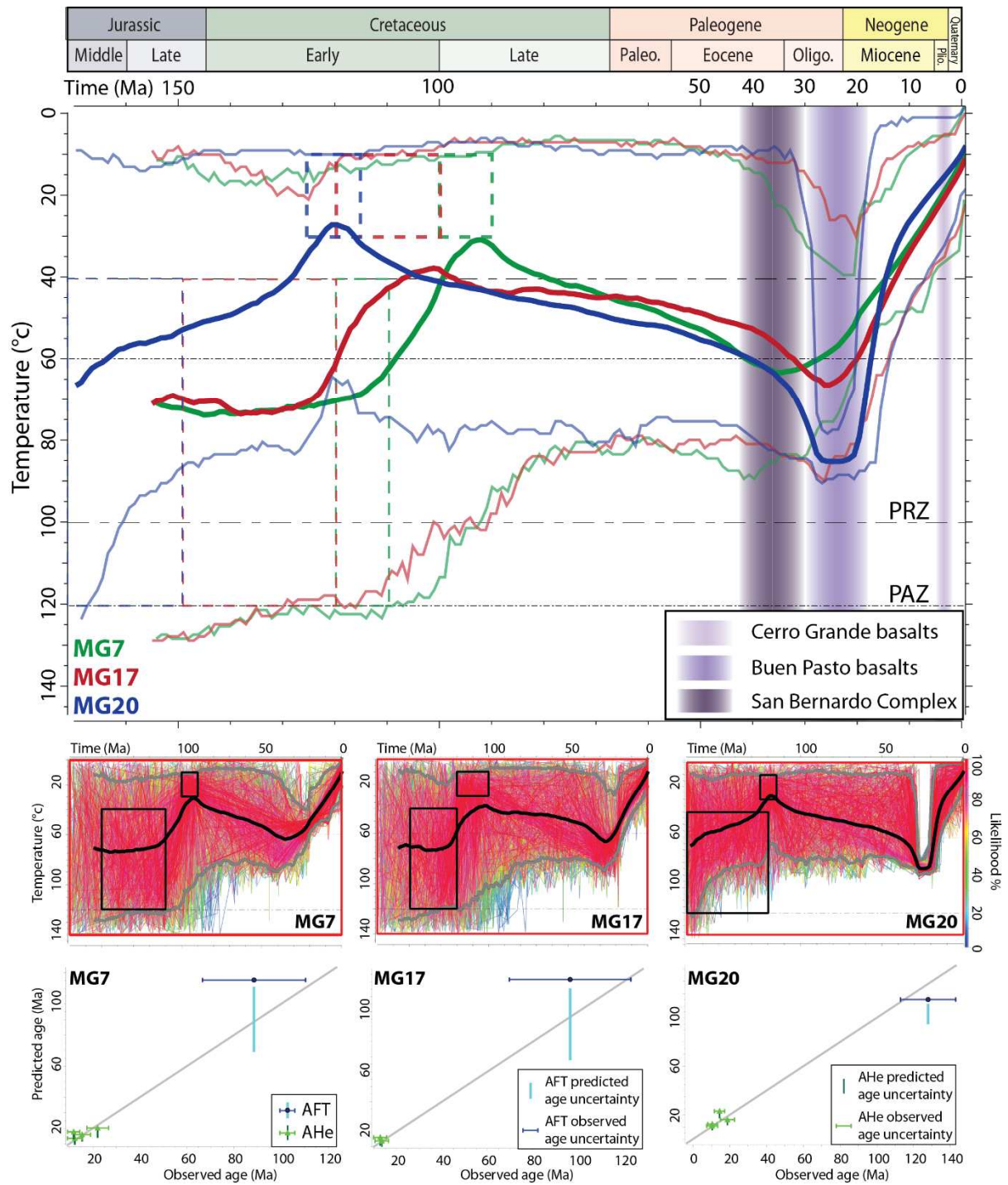


Figure 5.

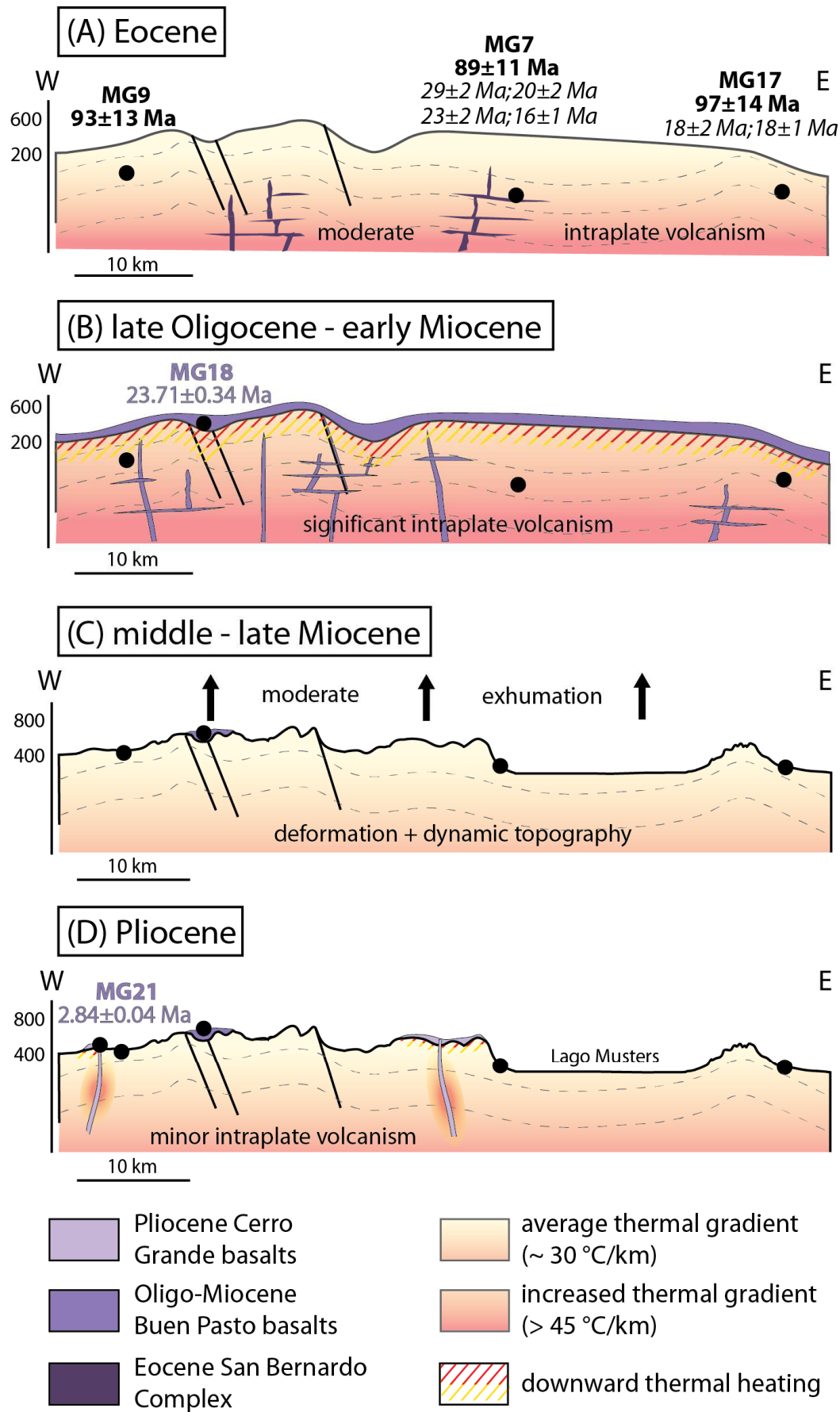


Figure 6.

## Tables

TABLE 1. SUMMARY OF SAMPLE INFORMATION AND APATITE FISSION TRACKS DATA

Samples <sup>†</sup>	Field*			Geology			Fission tracks data								
	Longitude	Latitude	Elev. (m)	Formation	Stratigr. age	n	<b>C. age</b>	$\sigma$	Ns	$\rho_s$	Ni	$\rho_i$	Nd	$\rho_D$	P( $\chi^2$ )
MG7	-69.2818	-45.5345	283	Bajo Barreal	Cenomanian	20	<b>88.5</b>	<b>11.4</b>	97	1.4	209	2.9	5000	11.1	100
MG9	-69.7016	-45.4590	557	Castillo	Aptian-Albian	10	<b>92.6</b>	<b>12.5</b>	88	2.5	178	5.1	5000	10.9	100
MG17	-69.0178	-45.4174	373	Castillo	Aptian-Albian	11	<b>96.7</b>	<b>13.8</b>	83	1.1	143	2.0	5000	9.7	100
MG20	-69.3007	-45.1388	568	Matasiete	Aptian	53	<b>128.0</b>	<b>8.7</b>	483	2.6	847	4.6	5000	13.1	100

\* longitude and latitude coordinates are given in WGS84

† Zeta=  $346 \pm 12$

N: number of apatite crystal counted; and  $\rho$ : track density ( $\times 10^5$  tracks/cm<sup>2</sup>); subscripts s, i and d denote spontaneous, induced and dosimeter, respectively; P( $\chi^2$ ): probability of obtaining a Chi-square value for n degrees of freedom.

**Table 1.** Apatite fission tracks data for the samples collected in the Chubut Group including samples location, sampled formations sampled and stratigraphic ages.

TABLE 2. APATITE (U-TH)/HE SINGLE-GRAIN DATA.

Sample	Longitude	Latitude	Elevation (m)	weight ( $\mu\text{g}$ )	$R_s$ ( $\mu\text{m}$ )	$F_T$	$^4\text{He}$ (ncc/g)	U (ppm)	Th (ppm)	Sm (ppm)	eU (ppm)	Th/U	AHe age (Ma)	Corrected AHe age	$\pm 1\sigma$ (Ma)
MG7B	-69.2818	-45.5345	283	2.3	62.1	0.77	22362	2.3	25.4	265.4	9	11.0	22.12	<b>28.7</b>	<b>2.3</b>
MG7C	-69.2818	-45.5345	283	1.0	45.2	0.69	18043	2.8	28.8	217.4	10	10.3	15.49	<b>22.5</b>	<b>1.8</b>
MG7D	-69.2818	-45.5345	283	1.1	36.6	0.63	15984	3.7	29.0	252.3	11	7.7	12.42	<b>19.6</b>	<b>1.6</b>
MG7E	-69.2818	-45.5345	283	2.2	55.1	0.74	11913	2.7	22.9	358.2	9	8.3	11.96	<b>16.1</b>	<b>1.3</b>
MG17A	-69.0178	-45.4174	373	4.1	58.9	0.74	8915	2.4	13.0	134.1	6	5.5	13.52	<b>18.2</b>	<b>1.5</b>
MG17C	-69.0178	-45.4174	373	3.9	53.0	0.72	15715	3.9	25.8	380.5	10	6.5	12.84	<b>17.8</b>	<b>1.4</b>
MG20A	-69.3007	-45.1388	568	1.7	44.7	0.66	21273	5.8	46.1	647.3	17	7.9	10.45	<b>15.9</b>	<b>1.3</b>
MG20B	-69.3007	-45.1388	568	9.1	90.9	0.83	67143	16.2	94.3	179.6	39	5.8	14.43	<b>17.3</b>	<b>1.4</b>
MG20D	-69.3007	-45.1388	568	0.9	32.8	0.56	39320	11.0	85.2	687.9	32	7.7	10.39	<b>18.5</b>	<b>1.5</b>
MG20G	-69.3007	-45.1388	568	5.4	69.7	0.79	58989	13.0	55.0	175.7	26	4.2	18.72	<b>23.7</b>	<b>1.9</b>

Note:  $R_s$ : sphere equivalent radius of hexagonal crystal with the same surface/volume ratio;  $F_T$ : geometric correction factor for age calculation; eU: effective uranium concentration.

**Table 2.** Apatite (U-Th-Sm)/He single-grain data results. AHe ages corrected using the ejection factor  $F_T$  (determined using the Monte Carlo simulation of Ketcham et al., 2011). Equivalent-sphere radius  $R_s$  calculated using procedure of Gautheron and Tassan-Got (2010). eU is the effective uranium concentration in ppm. Corrected ages given at  $1\sigma$  error.

TABLE 3. K-AR DATA.

Sample	Field (WGS84)			experiment no.	weight fused (g)	K (wt.%)	<sup>40</sup> Ar* (%)	<sup>40</sup> Ar* E+12 (at/g)	Age ± 1σ (Ma)	Weighted mean age ± 1σ (Ma)
	Longitude	Latitude	Elev. (m)							
MG18	-69.4250	-45.0682	739	5654	0.50052	1.188	62.9	29.348	23.50 ± 0.33	
(Buen Pasto)				5668	0.40044	1.188	64.9	29.862	23.91 ± 0.34	23.71 ± 0.34
MG21	-69.7130	-45.4616	582	5655	0.49925	1.79	46.7	5.3165	2.84 ± 0.04	
(Cerro Grande)				5667	1.4048	1.79	56.9	5.3209	2.84 ± 0.04	2.84 ± 0.04

**Table 3.** K-Ar dating results.